



UNIVERSITY OF LEEDS

This is a repository copy of *DEM and experimental study of bi-directional simple shear*.

White Rose Research Online URL for this paper:

<http://eprints.whiterose.ac.uk/147686/>

Version: Accepted Version

Article:

Zhang, M, Yang, Y, Zhang, H et al. (1 more author) (2019) DEM and experimental study of bi-directional simple shear. *Granular Matter*, 21 (2). 24. ISSN 1434-5021

<https://doi.org/10.1007/s10035-019-0870-1>

© Springer-Verlag GmbH Germany, part of Springer Nature, 2019. This is an author produced version of an article published in *Granular Matter*. Uploaded in accordance with the publisher's self-archiving policy.

Reuse

Items deposited in White Rose Research Online are protected by copyright, with all rights reserved unless indicated otherwise. They may be downloaded and/or printed for private study, or other acts as permitted by national copyright laws. The publisher or other rights holders may allow further reproduction and re-use of the full text version. This is indicated by the licence information on the White Rose Research Online record for the item.

Takedown

If you consider content in White Rose Research Online to be in breach of UK law, please notify us by emailing eprints@whiterose.ac.uk including the URL of the record and the reason for the withdrawal request.



eprints@whiterose.ac.uk
<https://eprints.whiterose.ac.uk/>

DEM and Experimental Study of Bi-directional Simple Shear

Min Zhang¹, Yunming Yang^{1,*}, Hanwen Zhang¹, Hai-Sui Yu²

¹ Department of Civil Engineering, Ningbo Nottingham New Materials Institute, University of Nottingham Ningbo, 199 Taikang East Road, Ningbo 315100, China

² School of Civil Engineering, University of Leeds, Leeds LS2 9JT, UK

Corresponding author: Dr. Yunming Yang* Email: Ming.Yang@nottingham.edu.cn Tel: +86 (0)574 88182407

Abstract

Stress-strain responses of granular material under bi-directional simple shear are comprehensively studied experimentally and numerically. The variable direction dynamic cyclic simple shear (VDDCSS) apparatus is used to test glass beads under various loading paths, and the DEM is used to reproduce experimental results. These two methods are complementary to each other. The glass beads are subject to the first shearing until a specified shear strain is reached, followed by the second shearing until the failure of samples, and the two shears are at various angles. The experimental results are in good agreement with the numerical results. Both experimental and numerical studies indicate that the development of shear stresses is dependent on the angle between the two shears in the early stage, and they approach the same ultimate values at the failure. The lateral stress, principal stress and non-coaxiality are also studied in the DEM simulation. While the lateral stress and principal stress are dependent on the angle, the orientations of principal stresses and plastic strain rate almost reach the same value at the failure. The contact force network and material fabric are also investigated to provide insight into the micro-scale responses and macro-micro relations regarding bi-directional simple shear.

Key words: Discrete element method; bi-directional simple shear; lateral stress; principal stress rotation; non-coaxiality; material fabric

Introduction

It has been well established that the principal stress rotation (PSR) leads to plastic volumetric strain and the non-coaxiality between the principal stress and plastic strain rate (Roscoe 1953; Bjerrum and Landva 1966; Oda and Konishi 1974). Because the PSR occurs in many geotechnical engineering applications, its impact on soil stress-strain responses has been comprehensively studied in experimental, theoretical and numerical aspects. Commonly used experimental facilities include the simple shear apparatus (Roscoe 1953; Bjerrum and Landva 1966) and the hollow cylinder apparatus (Hight et al. 1983). The former is mainly used in early years. Because it is generally not able to measure and control lateral normal stresses and strains (Budhu 1985), its applications are limited. The latter is able to control all three normal stresses and one shear stress, and it is widely used to study impacts of various factors on soil behavior under the PSR including anisotropy, intermediate principal stress, and other various stress paths, etc. The impact of PSR is also studied by using micro-mechanics and elastoplasticity (Spencer 1964; Rudnicki and Rice 1975; Christoffersen et al. 1981; Yu and Yuan 2006; Yang and Yu 2006). For instance, in the yield vertex theory, an additional plastic strain rate tangential to a yield surface is created by the PSR on the deviatoric plane (Rudnicki and Rice 1975). In other elastoplastic models, the PSR induced stress rate is considered by separate hardening rules and flow rules from those for the non-PSR stress rate. These elastoplastic models are also implemented into the finite element method to study the impact of PSR on geotechnical engineering applications including wave-seabed soil interactions and earthquake-induced soil liquefaction, and these numerical studies are compared with centrifuge test results (Sassa and Sekiguchi 2001; Wang et al. 2017). These studies indicate that ignoring or inadequately modeling the PSR impact can lead to unsafe results. Another method to study the PSR impact is the discrete element method (DEM), which is able to reflect the discrete characteristics of granular materials (Cundall and Strack 1979). The 2D and 3D DEM have been employed to model simple shear tests and hollow cylinder tests (Jiang et al. 2015; Thornton and Zhang 2006; Dabeet et al. 2015; Adhikari and You 2016; Asadzadeh and Soroush 2016; Farhang and Mirghasemi 2017). While the numerical results are generally in good agreement with experimental results, it can also study particle interactions such as the development of fabric. Another advantage of the DEM study is that it is able to study the development of lateral normal stresses in the simple shear test, which is difficult to be measured in the test.

Most of the studies mentioned above focus on only one shear or the PSR along one direction. However, in reality, soil is subjected to more than one shear in many geotechnical engineering applications. One example is the soil in an embankment under earthquake loading. The soil is subjected to one static shear stress from its self-weight, and it is subjected to the second dynamic shear stress from the earthquake loading. These two shear stresses generally are not along the same direction, and the shear stress from the earthquake loading is continually changing during an earthquake. An appropriate facility to study this behavior is the bi-directional simple shear tester (Ishihara and Yamazaki 1980; Rutherford 2012; Kammerer et al. 2002), which can impose two shears independently along two horizontal directions. Experimental results indicate that different angles between these two shears lead to different responses. However, an important drawback for the simple shear apparatus is the difficulty to

measure and control its lateral normal stresses. In this regard, the DEM can compensate for it because the lateral normal stresses can be computed from the interactions between particles in the model. The micro-scale responses with regard to bi-directional simple shear can also be investigated using the DEM. This study aims at comprehensively investigating the mechanical responses of glass beads in dense packing under bi-directional simple shear experimentally and numerically. For ease of computation and comparison, glass beads are used in the study, and the drained condition is considered. In this paper, the details of experimental setup and numerical implementation are given in the methodology. Then the stress-strain responses under bi-directional simple shear are presented, followed by the discussion of principal stress results. The characteristics of micro-scale contacts and material fabric are finally discussed by examining the contact force network, coordination number, and fabric tensor for the granular assemblies.

Methodology

The simple shear test is carried out by using the variable direction dynamic cyclic simple shear (VDDCSS) apparatus, as shown in Fig. 1. The experimental specimen is cylindrical and surrounded by a stack of low-friction Teflon-coated rings (each ring is 1 mm high) with an effective height of 21.6 mm and an effective diameter of 70mm. Three electromechanical load cells are used on the VDDCSS to apply stress or velocities to the specimen. The vertical Load cell applies vertical stress or velocities to the specimen, whereas the other two horizontal load cells apply horizontal stresses or velocities to the specimen. The two horizontal load cells enable the VDDCSS to perform simple shear in any horizontal direction. Thus, the vertical stress is exerted by the top load cell and maintained at a constant of 200 kPa in the study. Two horizontal shears are exerted on the specimen independently by two horizontal load cells. For ease of numerical simulations, the drained condition is considered. Li et al. (2016) gave more detailed information about the testing facility and procedure. Mono-sized glass beads are used in the test and its average diameter is 0.65 mm. Its density and initial porosity in the test are 2550 kg/m³ and 0.35, respectively. Its loading paths are shown in Fig. 2. Two shears are applied on the sample. The first shearing is exerted until a specified shear strain is reached, followed by the second shearing until the failure of samples. These two shears have various angles from 0⁰ to 180⁰ with an interval of 300, as shown in Fig. 2. Thus, the first shearing involves two directions xz and yz, and the second shearing has only one direction xz. To facilitate the comparison with the DEM simulation, the strain-controlled loading is used in the experiments. The shear velocity is 0.1mm/min, and the first shearing is exerted until its total shear strain reaches 2%.

The DEM model simulates the test performance as closely as possible. The three-dimensional (3D) particle flow code (PFC) (Itasca Consulting Group Inc. 2014) based on DEM is used to simulate the simple shear tests. Fig. 3(a) shows the 3D DEM model. The boundary of particulate DEM model consists of the top wall, bottom wall and cylindrical sidewall, which represent the top cap, bottom pedestal and ring-shaped side boundary of the VDDCSS, respectively. Similar to the test performance, the top wall is used to exert the constant vertical stress, and the side wall is displaced exerting the shear stress in the granular material. It has been verified by the authors that DEM results are rarely affected when the shear velocity ranges from 0.02mm/min to 0.2

mm/min. Thus, 0.2mm/min is used as the shear velocity in DEM simulations to improve the speed of calculation. In the DEM study, the sample is also firstly sheared to a shear strain of 2%, followed by the second shearing to the failure. The angles between these two shearing are the same as those in the test.

To reach the target porosity used in the test before shearing and consolidation, the overlapping method is used to prepare samples filled with spherical particles. The program of PFC 5.0 (Itasca Consulting Group Inc. 2014) will automatically calculate the particle number needed by the system based on input particle size distribution and porosity. Large overlaps between particles will be allowed during the generation of particles. As the initial equilibrium calculation starts, the large overlaps will be rapidly reduced to an allowable default value. When the bulk volume of a DEM model remains the same, the volume of all particles or voids remains unchanged as well during the equilibrium process although the particles are rearranged. Thus, the porosity, which is the ratio of the volume of voids to that of the bulk volume, generally remains to be 0.35 during the equilibrium process. It has been suggested by many researchers that the particle size can be scaled up to reduce the computational cost (Coetzee 2017), which will not significantly affect the results. For instance, in the DEM study conducted by Ni et al. (2000), the particle size in the DEM model was 2.5 times that of the material in reality. Similarly, Li et al. (2017) as well as Farhang and Mirghasemi (2017), scaled up the size of DEM particles by no less than 3 times. Accordingly, the particle size for the DEM models is set to be 2.5 times larger in our study, which results in approximately 30, 000 particles. The particle interaction is simulated by the rolling resistance linear model in PFC 5.0, which is actually a linear contact model with a rolling resistance coefficient in the software. Similar contact models have been introduced or validated by many researcher for cohesionless materials including glass beads and sand (Iwashita and Oda 1998; Tordesillas and Walsh 2002; Zhou et al. 2002). The DEM parameters used in the study are shown in Table 1, by referring to micromechanical parameters for glass beads or similar materials determined by Härtl and Ooi (2008) and other researchers (Ni et al. 2000; Shen et al. 2011; Dabeet et al. 2015; Asadzadeh and Soroush 2016; Li et al. 2017). The values of all parameters except for the final friction coefficient are set and added in the model before the equilibrium calculation is launched. The final friction coefficient is used after the equilibrium process is finished, which has been a well established way to simulate dense samples because a very small sliding coefficient can speed up the equilibrium calculation (O'Sullivan et al. 2004; Asadzadeh and Soroush 2016; Li et al. 2017).

The measurement sphere has long been used and well accepted by other researchers to obtain quantities such as stresses or strains (Asadzadeh and Soroush 2016). It is a sphere in three-dimensional model or a circle in two-dimensional model located in the DEM model. The measurement sphere will automatically measure the stress, strain rates, porosities of particles encircled by it without interfering with the calculation of software. In the DEM model of this paper, the measurement spheres are also used to measure the lateral normal stresses of side wall of irregular shape and strain rates. Fig. 3(b) shows nine measurement spheres initially generated in the study. The results indicate that the sphere 9 gives the most reliable and stable results. Budhu (1984) found that the stress and strain non-uniformities can develop and grow with shearing in monotonic loading. Since the non-

uniformities are directly influenced by the boundary condition, the sphere 9 is used to capture the development of lateral normal stresses and strain rates because it is the farthest to the boundary and has the minimum boundary effect. The shear strain and volumetric strain are obtained by dividing the horizontal displacement and vertical displacement by the height of the sample. The vertical stress, shear stress are obtained by tracing the average normal stress and average shear stress on the top wall, respectively. The equation for calculating the shear stress is given below. Where τ_{iz} denotes τ_{xz} and τ_{xy} , respectively. F_j^{ci} is the contact force for the j th particle with the top wall along the directions xz and yz , respectively. n is the total contact number on the top wall. A_{top} and r_{top} are the area and radius of the top wall, respectively.

$$\tau_{iz} = \frac{\sum_{j=1}^n F_j^{ci}}{A_{top}} = \frac{\sum_{j=1}^n F_j^{ci}}{\pi r_{top}^2} \quad (1)$$

Simple shear results and analyses

The study is first carried out under the simple shear along one direction to validate the discrete element modelling. The vertical stress for both experiments and DEM simulations is 200kPa, which remains unchanged as the shearing progresses. Fig. 4 shows the experimental and numerical development of the shear stress and volumetric strain with the shear strain until the failure. Fig. 4(a) shows the shear stress-strain response, in which the experimental result is in very good agreement with the numerical result. The sample of glass beads reaches its peak shear stress of approximately 80 kPa at a large shear strain, followed by a slight drop of shear stress. It is softer and more ductile than a particulate assembly of sand as the glass beads are spherical and of more uniform size than sands. Fig. 4(b) shows the volumetric strain response with shear strain. Given the fact that it is more difficult for the simulation to reproduce the volumetric strain in the experiment, the numerical and experimental results are in reasonably good agreement. Especially, the trend of the volumetric contraction followed by the expansion is well captured in the simulation.

Fig. 5 shows the experimental and numerical response of the shear stress τ_{xz} , τ_{yz} and the volumetric strain with the shear strain γ_{xz} at different angles between the first and second shearing. The first shearing is imposed until its total shear strain reaches 2%. The numerical results and the experimental results are in very good agreement at all angles. Fig. 5(a) and (b) show the development of the shear stresses τ_{xz} in experiments and DEM simulations, respectively. In Fig. 5(a) and (b), when the angle is larger than 90° , the shear stress τ_{xz} is increased in the negative direction during the first shearing, followed by a turning and an increase in the positive direction when the second shearing starts, because one component of the first shearing goes along the negative x -direction shown in Fig. 2. When γ_{xz} goes back to the origin in the shearing of larger than 90° , a positive τ_{xz} has already developed. As a result, a larger angle generally leads to a greater τ_{xz} at the origin. When the angle is smaller than 90° , γ_{xz} is always positive, and a larger angle generally leads to a lower τ_{xz} at a relatively small shear strain. However, with the increasing γ_{xz} during

the second shearing, τ_{xz} with different angles approach each other and eventually reach the same ultimate value at failure of approximately 80 kPa. The DEM simulations capture the trend and magnitude of the experimental results very well.

Fig. 5(c) and (d) show the development of the shear stress τ_{yz} with γ_{xz} . τ_{yz} starts at the value of 0 kPa at the beginning of the first shearing. It is obvious that the angle of 90° leads to the largest τ_{yz} and no γ_{xz} during the first shearing. The largest τ_{yz} is as high as 52 kPa at the angle of 90° , which is much lower compared with the ultimate shear strength of 80 kPa in Fig. 5(a) and (b). Similarly, an angle closer to 90° leads to a larger τ_{yz} smaller γ_{xz} during the first shearing during the first shearing. After it is taken over by the second shearing along the x-direction, τ_{yz} starts to decrease although γ_{xz} generated from the first shearing remains unchanged, and τ_{yz} eventually reaches zero at the failure where τ_{xz} reaches its ultimate value. The DEM simulations also reproduce the trend and values of the experimental results very well. Fig. 5(e) and (f) show the volumetric responses with γ_{xz} . The DEM simulations are also in very good agreement with the experimental results. The results indicate that the volume first decreases, followed by an increase at a relatively large shear strain. It is obvious in these figures that a larger angle leads to a larger volumetric contraction. This is because the angle results in an additional shearing from the shear strain γ_{yz} or negative γ_{xz} or both from the first shearing. The additional shearing within a range of a relatively small shear strain leads to more contraction of the sample. A larger angle results in a larger additional shearing, which is reflected by a larger volumetric contraction when γ_{xz} is at the origin. From Figure 4 and 5, it can be concluded that DEM results are in reasonably good agreement with experimental results. The slight differences between them do not obviously influence the qualitative analysis, which has been demonstrated by previous research (O'Sullivan 2004; Dabeet et al. 2015; Asadzadeh and Soroush 2016).

While it is difficult for the tests to measure the lateral normal stress in the sample, the DEM simulation can calculate the lateral normal stress by using the measurement sphere. Fig. 6 shows the calculated lateral normal stresses σ_x and σ_y with γ_{xz} . Because the DEM results are in very good agreement with the experimental results of the shear stresses along two directions and the volumetric strain, it can be inferred that the calculated lateral normal stresses closely reproduce the actual values. Fig. 6(a) for σ_x indicates that its initial value is 52 kPa before the shearing starts at all the angles before the shearing starts. The first shearing makes σ_x increase. When γ_{xz} returns to the origin, a larger angle leads to a larger σ_x because a larger angle generates a larger additional shearing. The increase rate of σ_x is almost the same for all the angles during the second shearing. Thus, the value of σ_x at a larger angle is generally higher than that at a smaller angle. With increasing γ_{xz} , σ_x approaches 200 kPa which is exactly the value of vertical stress. The development of σ_y in Fig. 6(b) is similar to that for σ_x . Its initial value is also 52 kPa and the first shearing at a larger angle generates a larger value of σ_y . The increase rate of σ_y is almost the same at all the angles during the second shearing, and thus, a larger angle leads to a larger σ_y . On the other hand, the increase rate of σ_y is smaller than that for σ_x , and σ_y approaches 140 kPa. Consequently, σ_x is associated with the second shearing and σ_y is associated with the first shearing ending at a shearing strain of 2%.

Given the vertical and two lateral normal stresses and two shear stresses in the DEM simulations, the principal stresses can be determined. Fig. 7 shows the development of three principal stresses with γ_{xz} . There are peaks, valleys and turning for the early development of principal stresses, and they are more notable for the minor principal stress. It is because τ_{xz} experiences a negative increase during the first shearing, followed by a positive increase during the second shearing at the angles larger than 90° , shown in Fig. 5(a) and (b). Similarly, τ_{yz} experiences an increase to a peak, followed by a remarkable drop for all the angles, as shown in Fig. 5(c) and (d). Fig. 7 indicates that a larger angle generally leads to a greater principal stress for three principal stresses. The reason is that a larger angle leads to larger shear stress and a larger lateral stresses. Fig. 8 shows the orientations of principal stresses and major principal strain rate during the second shearing. The orientations of principal stresses and strain rates are the angles with regard to the z-axis. Although it is more difficult for the DEM simulations to extract the orientation of strain rate, the general trend is that these two orientations are non-coaxial for all the angles. With increasing shear strain, the non-coaxiality becomes smaller, and eventually they almost approach the same orientation at the end of shearing. This is consistent with the principle of non-coaxiality for the shearing along one direction as was observed in previous studies (Yang and Yu 2006; Thornton and Zhang 2006; Ai et al. 2014; Asadzadeh and Soroush 2016). The reason may be that the second shearing along only the x-direction is dominant during the whole loading process.

Contact force network and material fabric

The contact force network can be used to show the distribution of micro-scale contacts and transmission of contact forces. Taking the contact force network at 60° as an example, Fig. 9 shows the front view (xz-plane), side view (yz-plane) and top view (xy-plane) of contact force chains in the 3D DEM model. The thickness of the black lines is proportional to the magnitude of contact forces and the orientation of the black lines denotes the direction of contact normals. From the contact force chains on the left in Fig. 9 (a) to (c), it can be seen that the contact forces are randomly orientated after consolidation, and the contact force network is generally transversely isotropic (cross-anisotropic). After the first shearing, contact force chains projected on the xz and yz plane slightly incline towards the diagonal direction due to the development of γ_{xz} and γ_{yz} . The transverse isotropy of contact force network does not change much. However, at the end of the second shearing, the strong contact forces (darker and wider lines) are remarkably focused on the dominant directions. For instance, in Fig. 9(a), the strong contact forces projected on the xz plane approach a notable diagonal distribution, similar to the distribution under unidirectional shear obtained by Thornton and Zhang (2006), Shen et al. (2011) and Asadzadeh and Soroush (2016). In Fig. 9(b), strong contact forces projected on the yz plane are vertically dominant while in Fig. 9(c), on the xy-plane, the strong contact forces are dominantly orientated in the x-direction. The distribution of the magnitude of contact forces thus, becomes orthotropic at the end of the second shearing. The dominance of contact forces in the x-direction over the y-direction is consistent with the development of two shear stresses in Fig. 5, where the shear stress τ_{xz} keeps increasing and the shear stress τ_{yz} gradually diminishes with the progress of the second shearing.

Fig. 10(a) and (b) show the quantitative distribution of the magnitude and normal of contact forces, respectively. A bin indicates that the distribution direction of the magnitude or the normal of contact forces increases by 5° in the rose diagram. The orthotropic anisotropy of the magnitude of contact forces can be further observed in Fig. 10 (a). Fig. 10 (b) illustrates that the distribution of contact normals can be approximated to be transverse isotropy because the rose diagram of contact normals projected on the xy plane is approximately circular. By comparing Fig. 10(a) with (b), the distribution of magnitude of contact forces is less uniform than that of the contact normals. Those contact normals orientated in the bins named as weak area only transmit weak forces that are lower than the average contact force even though they are in high proportions. In addition, Thornton and Zhang (2006) found that the normal of strong contact forces aligned with the directions of σ_1 under unidirectional simple shear. Under bi-directional simple shear, before the second shearing, the strong contact forces projected on vertical planes are not observed to align themselves with that of σ_1 in Fig. 8 because of the additional shear from γ_{yz} . Nevertheless, by the end of the second shearing, the orientation of σ_1 generally falls within the bins representing strong contact forces projected on the xz plane. Different from the relation between the orientation of σ_1 and that of strong contact forces on the xz plane, the strong contact forces on the yz plane are mainly orientated in or close to the vertical direction when the contact forces in the y-direction are remarkably weaker. This can explain why the τ_{yz} almost reaches zero in the end while the σ_z and τ_{xz} are very high. Fig. 11 shows the final distribution of the magnitude of contact forces projected on xz plane at the loading angle from 0° to 180° other than 60° . At different loading angles, a very similar distribution of the magnitudes of contact forces can be clearly observed. This provides micromechanical evidence for the phenomenon that the τ_{xz} for all angles as well as orientations of σ_1 almost reaches the same ultimate value.

The coordination number Z is commonly used to define the average density of contacts per particle within the granular material. Therefore, it has the ability to describe the packing intensity which is an important characteristic of the material fabric. The simplest definition of Z is given by

$$Z = \frac{2N_c}{N_p} \quad (2)$$

where N_c is the total number of contacts and N_p is the total number of particles. Fig. 12 shows the development of coordination number Z with shear strain in DEM simulations. For all loading angles, the coordination number Z has the same initial value of 7.35. When the loading angle is smaller than 90° , the value of Z increases with the first shearing and declines constantly with the second shearing. When the loading angle is larger than 90° , the value of coordination number Z increases in the negative direction during the first shearing, followed by a slight increase in the positive direction when the second shearing starts and a constant decline as the shearing progresses. At the end of the second shearing, the coordination number Z for different loading angles ends with the value between 6.63 and 6.7. By comparing the coordination number in Fig. 12 with the volumetric strain in Fig. 5, it can be illustrated that the coordination number generally increases with contraction of granular assembly and decreases

with assemblies' dilation. Thus, the coordination number is associated with the volumetric change, indicating the relation between macro-scale deformation and micro-scale structure regarding bi-directional shear.

To gain a deeper understanding of the material fabric, the fabric tensor (or anisotropy tensor) was defined by Satake (1982) as:

$$\Phi_{ij} = \frac{1}{N_c} \sum_{k=1}^{N_c} n_i^k n_j^k \quad (i, j = 1, 2, 3) \quad (3)$$

where n_i^k denotes the k-th contact normal vector within a granular assembly. Hence, this equation defines the fabric tensor from the perspective of the contact normal.

where $\cos\alpha_k$, $\cos\beta_k$ and $\cos\gamma_k$ denote direction cosines of the k-th contact. The three eigenvectors of Φ_{ij} are the orientations of the principal fabric, and the eigenvalues (Φ_1 , Φ_2 , Φ_3) indicate the magnitude of the principal fabric in each of these three directions. To accurately quantify the degree of fabric anisotropy, Barreto et al. (2009) proposed a general definition of deviator fabric as follows by using these three eigenvalues:

$$\Phi_d = \sqrt{\frac{(\Phi_1 - \Phi_2)^2 + (\Phi_2 - \Phi_3)^2 + (\Phi_3 - \Phi_1)^2}{2}} \quad (4)$$

Fig. 13 shows the development of the deviator fabric Φ_d and the orientations of the major principal fabric Φ_1 calculated by using the DEM orientation data. In Fig. 13(a), the Φ_d at different loading angles has the same initial value. The initial anisotropy comes from the inherent anisotropy caused by depositional process and the induced anisotropy caused by vertical consolidation. In general, the deviator fabric Φ_d increases with shearing, and the increase rate gradually declines. A larger loading angle generally leads to a higher degree of fabric anisotropy, but the deviator fabric almost reaches the same value by the end of shearing. In Fig. 13(b), the orientation of the major principal fabric Φ_1 almost has the same developing trend with the deviator fabric in Fig. 13(a). Its evolution also resembles that of the major principal stress σ_1 in Fig. 8 for all loading angles. However, it can be observed that the orientation of Φ_1 has a slightly lower value compared to that of the major principal stress σ_1 before a large shear strain of 15% is reached. This phenomenon was also observed by other researchers (Asadzadeh and Soroush 2016; Shen et al. 2011; Ai et al. 2014; Oda et al. 1980). The main reason for the slight difference between these two directions, as mentioned by Shen et al. (2011) and Asadzadeh and Soroush (2016), was that the larger contact forces gave a stronger contribution to the stress tensor while all contact forces contributed equally to the fabric tensor. In other words, the stress tensor considers the magnitude and normal of contact forces, while the fabric tensor only considers the contact normal and has nothing to do with the magnitude of contact forces. This can be further confirmed by the absence of the magnitude of contact forces and stress components in Equation (3) for the calculation of the fabric tensor.

Conclusions

This paper studies the mechanical responses of granular material in the simple shear tests by using the bi-directional simple shear tester and the DEM, with the focus on the shearing along two directions. The specimen is subject to two shears, and the first shearing is at various angles with the second shearing. The DEM simulation results are in very good agreement with the experimental results. Both experimental and numerical results indicate that although the shear stresses are dependent on the loading angles during the early stage of shearing, they all approach the same ultimate value at the failure of the specimen. Both results indicate that a larger angle leads to a larger volumetric contraction as a larger angle gives more shearing. While the simple shear tester is not able to measure the lateral normal stresses in the specimen, the DEM study can compensate for it and calculate them. The values of lateral normal stresses are dependent on the angle between two shears, and the larger the loading angles are, the higher the lateral normal stresses are. The principal stress can also be determined in the DEM study, and a larger angle leads to a larger principal stress. The orientation of the principal stress is different from that for the principal strain rate and the former is dependent on the loading angles. However, the non-coaxiality between them decreases with increasing shear strain, and these two orientations approach the same value at the failure of the specimen for all the angles. It is consistent with the principle of non-coaxiality for the simple shear along only one direction. The additional shearing from the shear strain γ_{yz} plays an important role in the relation between the normal of strong contact forces and the orientation of the major principal stress, mainly at the early stage of shearing. The distribution of the magnitude of contact forces evolves from initial transverse isotropy to orthotropic anisotropy in the end while the distribution of the contact normal generally remains transversely isotropic. Meanwhile, the distribution of the magnitude of contact forces is notably less uniform than that of the contact normal. The distributions of these two contact components also provide the micromechanical evidences for the macro-scale stress-strain responses. The material fabric including coordination number and fabric tensor is sensitive to the loading angles. It is shown that the coordination number has a close relation to the volumetric change, indicating the correlation between macro-scale deformation and micro-scale structure regarding bi-directional shear. The evolution of the orientation of the major principal fabric resembles that of the major principal stress for all angles. However, a slight difference between these two directions is observed, which can be largely attributed to the absence of the magnitude of contact forces and stress components for the calculation of the fabric tensor.

Acknowledgement

This work is supported by NSFC (Project code 11872219), Zhejiang Natural Science Foundation (project code LY18E090006) and the National Basic Research Program of China (Grant No. 2014CB047006). These supports are appreciated.

Compliance with Ethical Standards

Funding: This study was funded by NSFC (Project code 11872219), Zhejiang Natural Science Foundation (Project code LY18E090006) and the National Basic Research Program of China (Grant No. 2014CB047006).

Conflict of Interest: The authors declare that they have no conflict of interest.

(And/or in case humans were involved) Ethical approval: This article does not contain any studies with human participants or animals performed by any of the authors.

Informed consent: Informed consent is not obtained because individual participants are not included in the study.

References

- Adhikari, S., You, Z.P.: 3D discrete element models of the hollow cylindrical asphalt concrete specimens subject to the internal pressure. *International Journal of Pavement Engineering* 11(5), 429-439 (2010). doi:10.1080/10298436.2010.489114
- Ai, J., Langston, P.A., Yu, H.-S.: Discrete element modelling of material non-coaxiality in simple shear flows. *International Journal for Numerical and Analytical Methods in Geomechanics* 38(6), 615-635 (2014). doi:10.1002/nag.2230
- Asadzadeh, M., Soroush, A.: Fundamental investigation of constant stress simple shear test using DEM. *Powder Technology* 292, 129-139 (2016). doi:10.1016/j.powtec.2016.01.029
- Barreto, D., O'Sullivan, C., Zdravkovic, L., Nakagawa, M., Luding, S.: Quantifying the evolution of soil fabric under different stress paths. *Powders and Grains* 1145(1), 181-184 (2009). doi:10.1063/1.3179881
- Bjerrum, L., Landva, A.: Direct simple-shear tests on a norwegian quick clay. *Géotechnique* 16(1), 1-20 (1966). doi:10.1680/geot.1966.16.1.1
- Budhu, M.: Nonuniformities imposed by simple shear apparatus. *Canadian Geotechnical Journal* 21(1), 125-137 (1984). doi:10.1139/t84-010
- Budhu M.: Lateral stresses observed in two simple shear apparatus. *Journal of Geotechnical Engineering*, 111(6), 698-711 (1985). doi:10.1061/(ASCE)0733-9410(1985)111:6(698)
- Christoffersen, J., Mehrabadi, M.M., Nematnasser, S.: A micromechanical description of granular material behavior. *Journal of Applied Mechanics* 48(2), 339-344 (1981). doi:10.1115/1.3157619
- Cundall, P.A., Strack, O.D.L.: A discrete numerical model for granular assemblies. *Géotechnique* 29(1), 47-65 (1979). doi:10.1680/geot.1979.29.1.47
- Coetzee, C.J.: Review: Calibration of the discrete element method. *Powder Technology* 310, 104-142 (2017). doi:10.1016/j.powtec.2017.01.015
- Dabeet, A., Wijewickreme, D., Byrne, P.: Evaluation of stress strain non-uniformities in the laboratory direct simple shear test specimens using 3D discrete element analysis. *Geomechanics and Geoengineering* 10(4), 249-260 (2015). doi:10.1080/17486025.2014.979889
- Farhang, B., Mirghasemi, A.A.: A study of principle stress rotation on granular soils using DEM simulation of hollow cylinder test. *Advanced Powder Technology* 28(9), 2052-2064 (2017). doi:10.1016/j.appt.2017.05.011
- Hight, D.W., Gens, A., Symes, M.J.: The development of a new hollow cylinder apparatus for investigating the effects of principal stress rotation in soils. *Géotechnique* 33(4), 355-383 (1983). doi:10.1680/geot.1983.33.4.355
- Härtl, J., Ooi, J.Y.: Experiments and simulations of direct shear tests: porosity, contact friction and bulk friction. *Granular Matter* 10(4), 263-271 (2008). doi:10.1007/s10035-008-0085-3
- Ishihara, K., Yamazaki, F.: Cyclic simple shear tests on saturated sand in multi-directional loading. *Soils and Foundations* 20(1), 45-59 (1980). doi:10.3208/sandf1972.20.45
- Itasca Consulting Group Inc.: PFC (particle flow code in 2 and 3 dimensions), version 5.0 [User's manual]. Minneapolis (2014)
- Iwashita, K., Oda, M.: Rolling resistance at contacts in simulation of shear band development by DEM. *Journal of Engineering Mechanics* 124(3), 285-292 (1998). doi:10.1061/(ASCE)0733-9399(1998)124:3(285)
- Jiang, M.J., Harris, D., Yu, H.S.: Kinematic models for non-coaxial granular materials. Part II: evaluation. *International Journal for Numerical and Analytical Methods in Geomechanics* 29(7), 663-689 (2005). doi:10.1002/nag.431
- Kammerer, A.M., Pestana, J.M., Seed, R.B.: Undrained response of Monterey 030 sand under multidirectional cyclic simple shear loading conditions. University of California, Berkeley, (2002).
- Li, Y., Yang, Y., Yu, H.S., Roberts, G.: Monotonic direct simple shear tests on sand under multidirectional loading. *International Journal of Geomechanics* 17(1), 04016038 (2016). doi:10.1061/(asce)gm.1943-5622.0000673
- Li, B., Chen, L., Gutierrez, M.: Influence of the intermediate principal stress and principal stress direction on the mechanical behavior of cohesionless soils using the discrete element method. *Computers and Geotechnics* 86, 52-66 (2017). doi:10.1016/j.compgeo.2017.01.004
- Ni, Q., Powrie, W., Zhang, X.: Effect of particle properties on soil behaviour: 3-D numerical modelling of shear box tests. *Numerical methods in geotechnical engineering*, 58-70 (2000). doi:10.1061/40502(284)5
- Oda, M., Konishi, J.: Rotation of principal stresses in granular material during simple shear. *Soils and Foundations* 14(4), 39-53 (1974). doi: 10.3208/sandf1972.14.4_39
- Oda, M., Konishi, J., Nemat-Nasser, S.: Some experimentally based fundamental results on the mechanical behaviour of granular materials. *Géotechnique* 30(4), 479-495 (1980). doi:10.1680/geot.1980.30.4.479
- O'Sullivan, C., Cui, L., Bray, J.D.: Three-dimensional discrete element simulations of direct shear tests. *Numerical Modeling in Micromechanics via Particle Methods* 373-382 (2004).

Roscoe, K.H.: An apparatus for the application to simple shear to soil samples. In: Proceedings of the 2nd International Conference on Soil Mechanics and Foundation Engineering, pp. 186-191 (1953)

Rudnicki, J.W., Rice, J.R.: Conditions for the localization of deformation in pressure-sensitive dilatant materials. *Journal of the Mechanics and Physics of Solids* 23(6), 371-394 (1975). doi:10.1016/0022-5096(75)90001-0

Rutherford, C.: Development of a multi-directional direct simple shear testing device for characterization of the cyclic shear response of marine clays. Texas A&M University (2012)

Satake, M.: Fabric tensor in granular materials. In: IUTAM Conference on Deformation and Failure of Granular Materials, pp. 63-67 (1982)

Sassa, S., Sekiguchi, H.: Analysis of wave-induced liquefaction of sand beds. *Géotechnique* 51(2), 115-126 (2001). doi:DOI 10.1680/geot.51.2.115.40288

Spencer, A.J.M.: A theory of the kinematics of ideal soils under plane strain conditions. *Journal of the Mechanics and Physics of Solids* 12(5), 337-351 (1964). doi:10.1016/0022-5096(64)90029-8

Shen, C.K., O'Sullivan, C., Jardine, R.J.: A micromechanical investigation of drained simple shear tests. In: Proceedings of the 5th International Symposium on Deformation Characteristics of Geomaterials, pp. 314-321 (2011)

Thornton, C., Zhang, L.: A numerical examination of shear banding and simple shear non-coaxial flow rules. *Philosophical Magazine* 86(21-22), 3425-3452 (2006). doi:10.1080/14786430500197868

Tordesillas, A., Walsh, D.C.S.: Incorporating rolling resistance and contact anisotropy in micromechanical models of granular media. *Powder Technology* 124(1-2), 106-111 (2002). doi:10.1016/S0032-5910(01)00490-9

Wang, Z., Yang, Y.M., Yu, H.S.: Effects of principal stress rotation on the wave-seabed interactions. *Acta Geotechnica* 12(1), 97-106 (2017). doi:10.1007/s11440-016-0450-z

Yang, Y.M., Yu, H.S.: A non-coaxial critical state soil model and its application to simple shear simulations. *International Journal for Numerical and Analytical Methods in Geomechanics* 30(13), 1369-1390 (2006). doi:10.1002/nag.531

Yu, H.S., Yuan, X.: On a class of non-coaxial plasticity models for granular soils. In: Proceedings of the Royal Society a-Mathematical Physical and Engineering Sciences, vol. 2067, pp. 725-748 (2006)

Zhou, Y.C., Xu, B.H., Yu, A.B., Zulli, P.: An experimental and numerical study of the angle of repose of coarse spheres. *Powder Technology* 125(1), 45-54 (2002). doi:10.1016/S0032-5910(01)00520-4

Figure Captions

Fig. 1 Variable direction dynamic cyclic simple shear (VDDCSS) apparatus: (a) Overview of VDDCSS; (b) prepared glass beads; (c) installed specimen before consolidation

Fig. 2 Schematic diagram of loading directions in the simple shear test (a: unidirection; b: bi-direction)

Fig. 3 DEM model (a) and measurement spheres (b)

Fig. 4 Experimental and DEM results in the unidirectional shear tests (a: shear stress; b: volumetric strain)

Fig. 5 Stress-Strain responses of the experiments and DEM at different angles for the first shearing at 2% (a, c, e: experiments; b, d, f: DEM)

Fig. 6 Lateral normal stresses at different loading angles by the DEM (a: x-direction; b: y-direction)

Fig. 7 Principal stresses at different loading angles by the DEM (a: major; b: intermediate; c: minor)

Fig. 8 Orientations of major principal stresses and principal strain rates at different loading angles by the DEM

Fig. 9 Contact force chains of the 3D DEM model at the loading angle of 60° (a: front view (looking along the y-axis); b: side view (looking along the x-axis); c: top view (looking along the z-axis))

Fig. 10 Rose diagrams of the magnitude of contact forces (a) and contact normals (b) within the 3D DEM model by the end of the second shearing at the loading angle of 60°

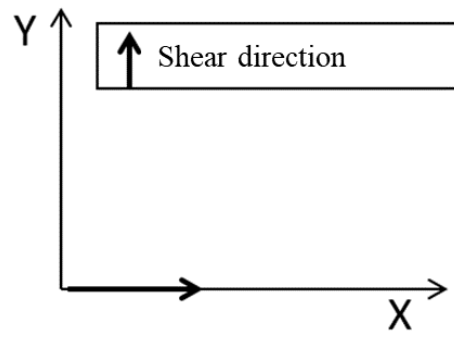
Fig. 11 Rose diagrams of the magnitude of contact forces projected on the xz-plane ($y = 0$) at the end of the second shearing at different loading angles

Fig. 12 Coordination number calculated by the DEM

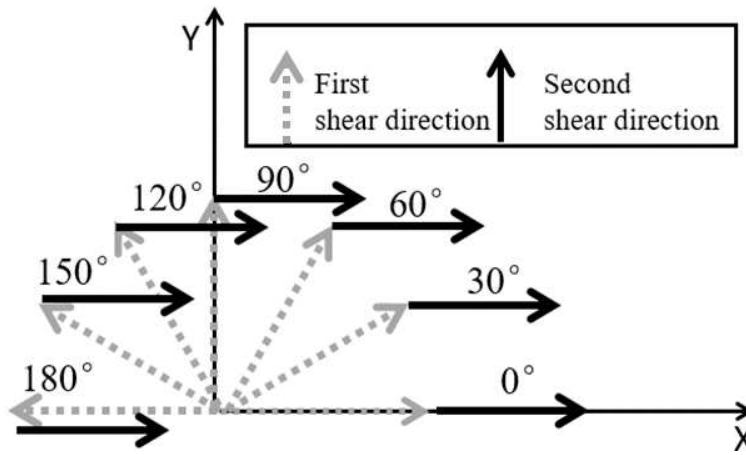
Fig. 13 Deviator fabric (a) and orientation of the major principal fabric (b) at different loading angles by the DEM



Fig. 1 Variable direction dynamic cyclic simple shear (VDDCSS) apparatus: (a) Overview of VDDCSS; (b) prepared glass beads; (c) installed specimen before consolidation

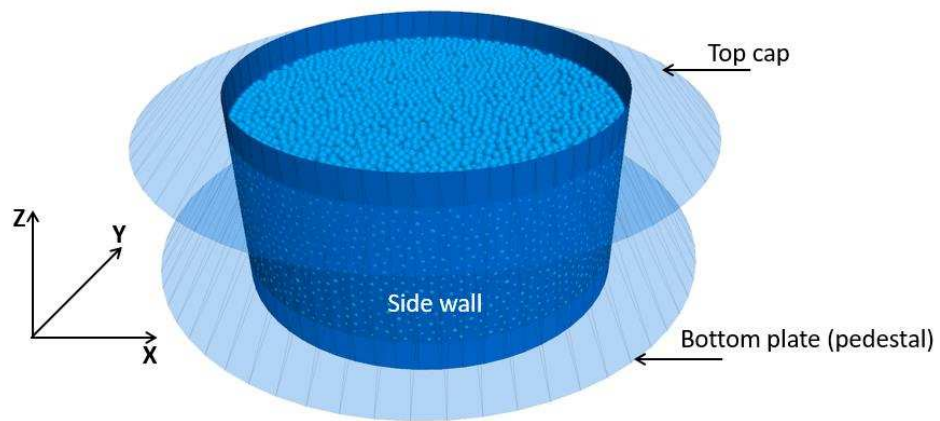


(a)

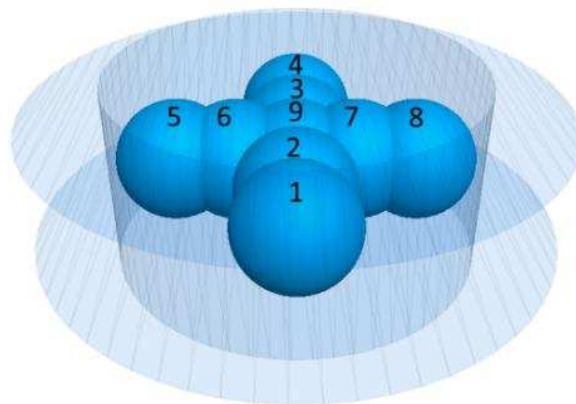


(b)

Fig. 2 Schematic diagram of loading directions in the simple shear test (a: unidirection; b: bi-direction)

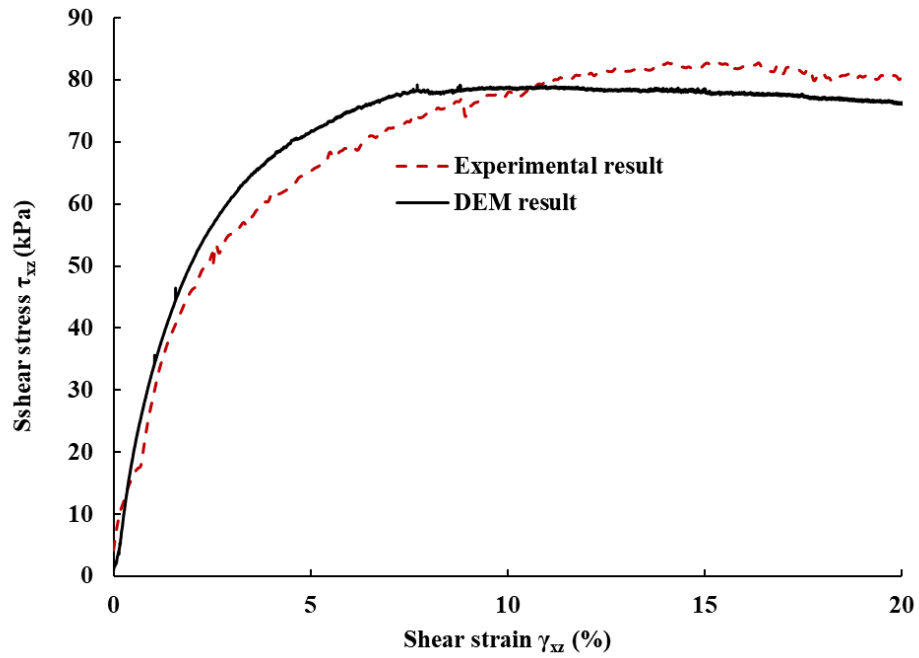


(a)

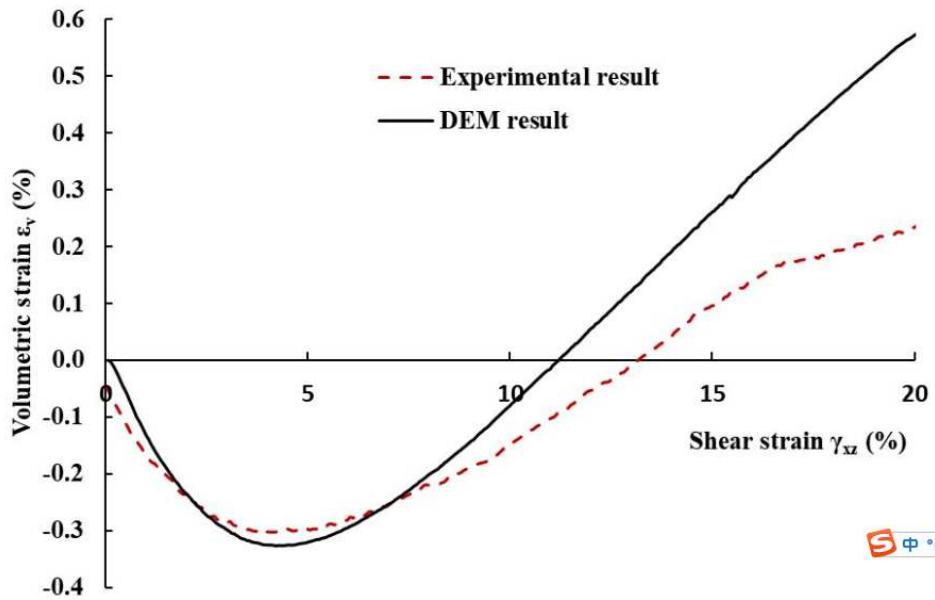


(b)

Fig. 3 DEM model (a) and measurement spheres (b)

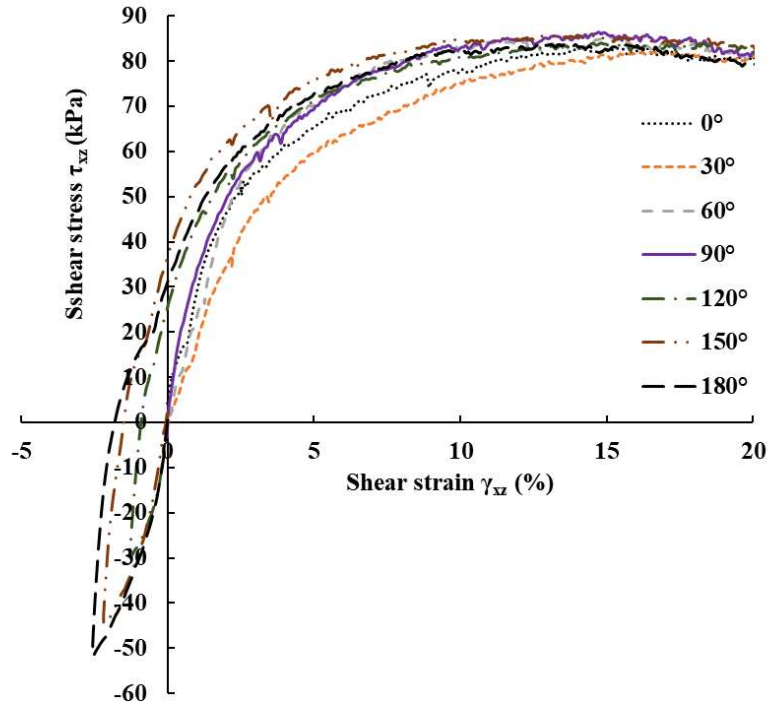


(a)

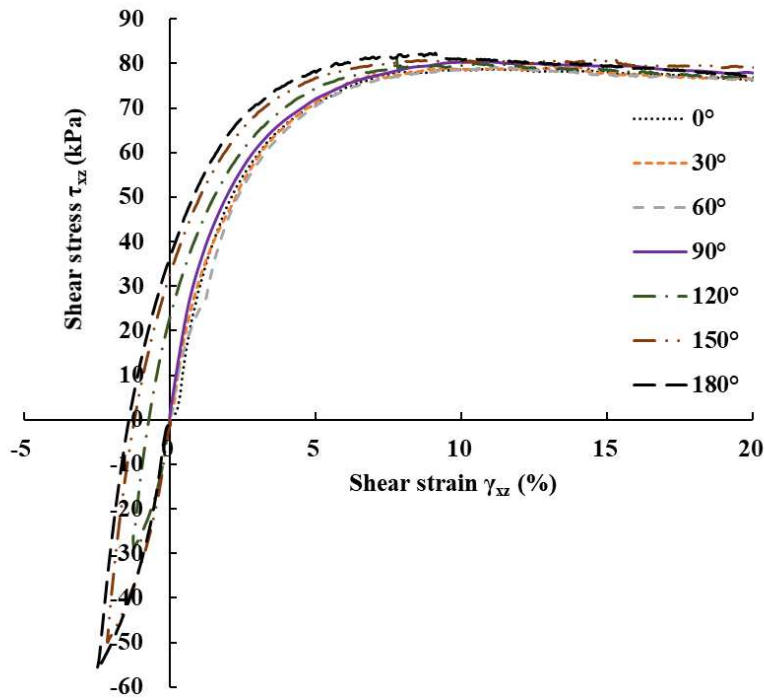


(b)

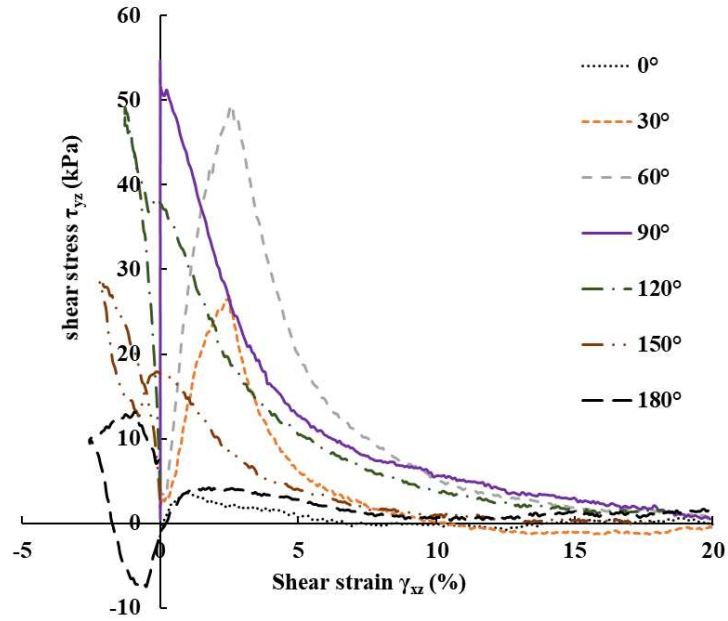
Fig. 4 Experimental and DEM results in the unidirectional shear tests (a: shear stress; b: volumetric strain)



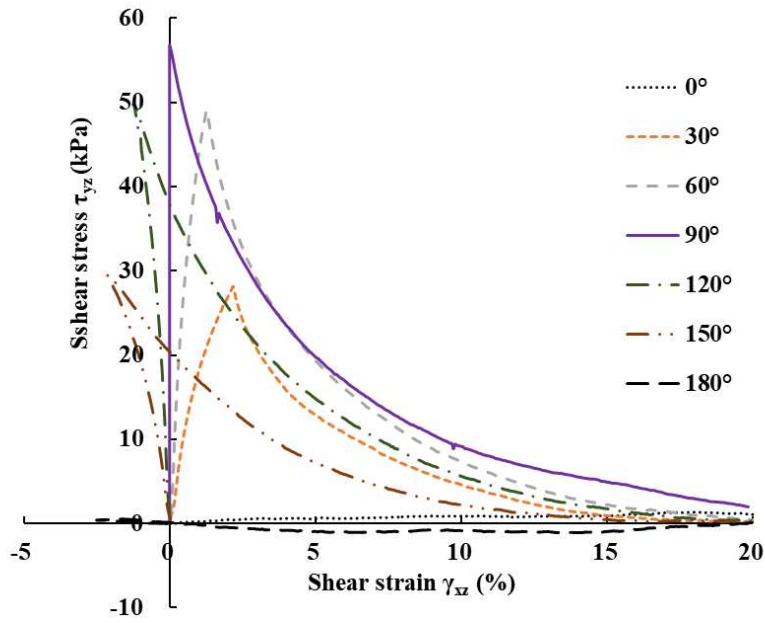
(a)



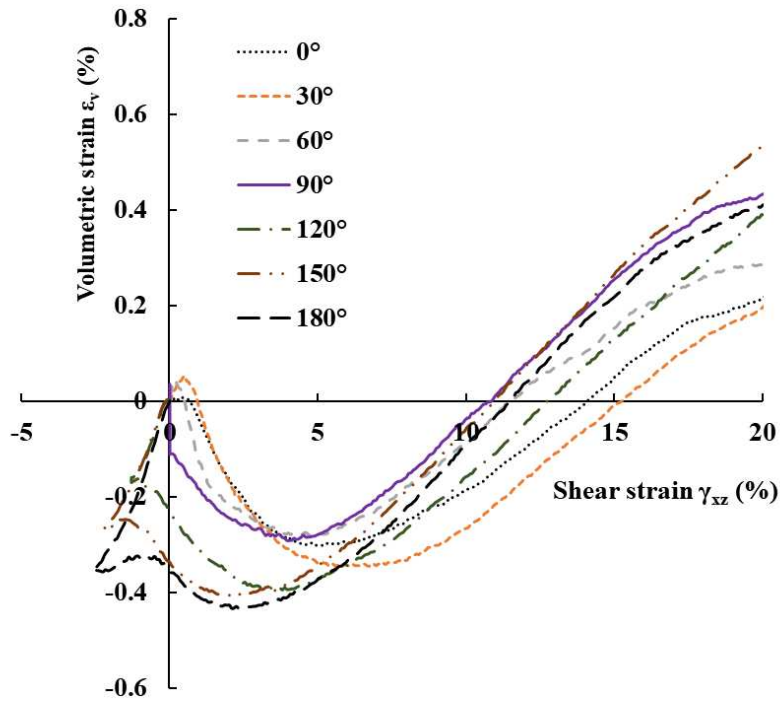
(b)



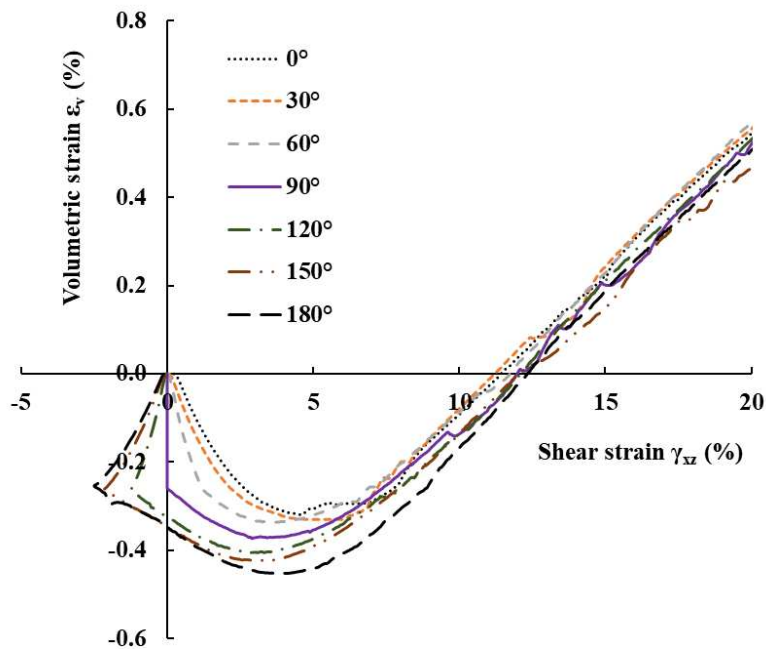
(c)



(d)

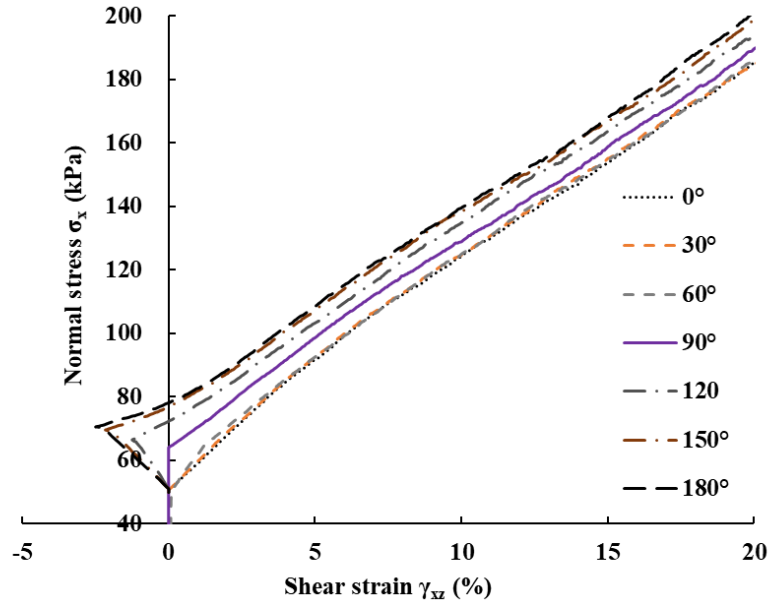


(e)

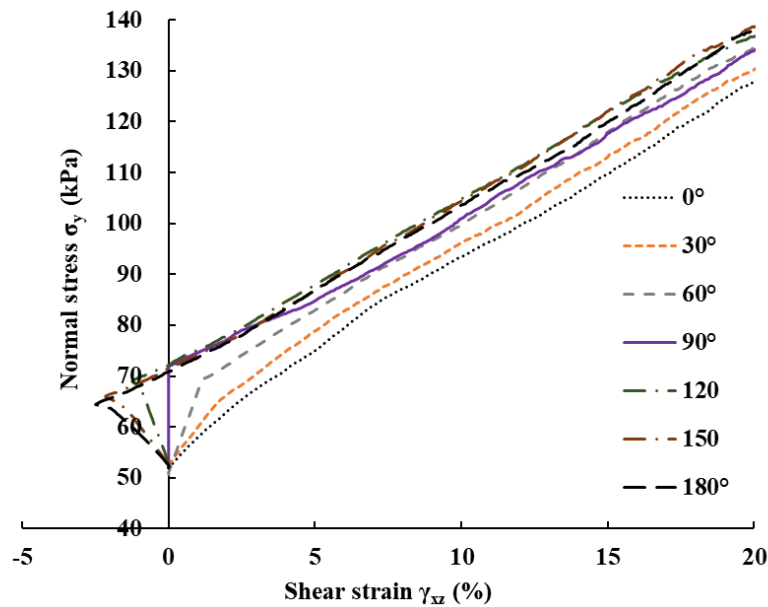


(f)

Fig. 5 Stress-Strain responses of the experiments and DEM at different angles for the first shearing at 2% (a, c, e: experiments; b, d, f: DEM)

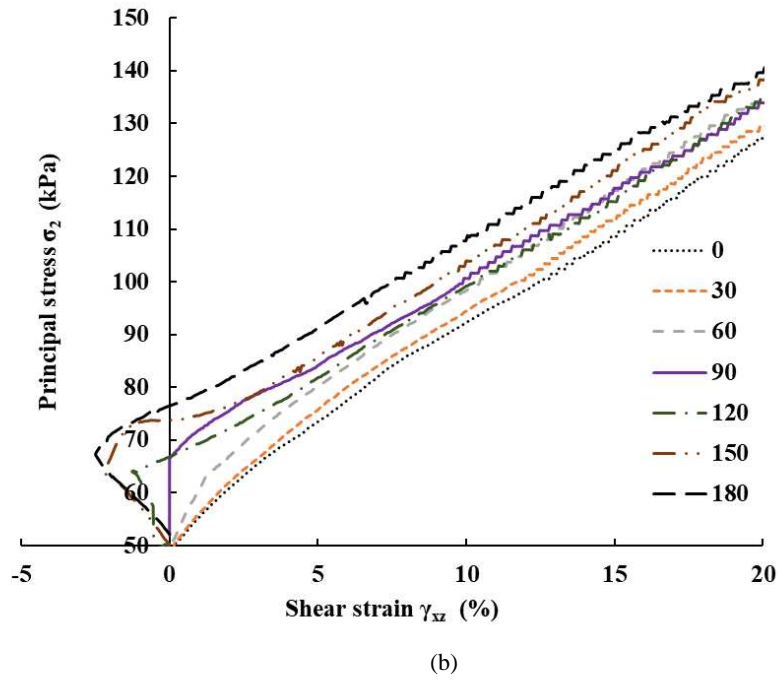
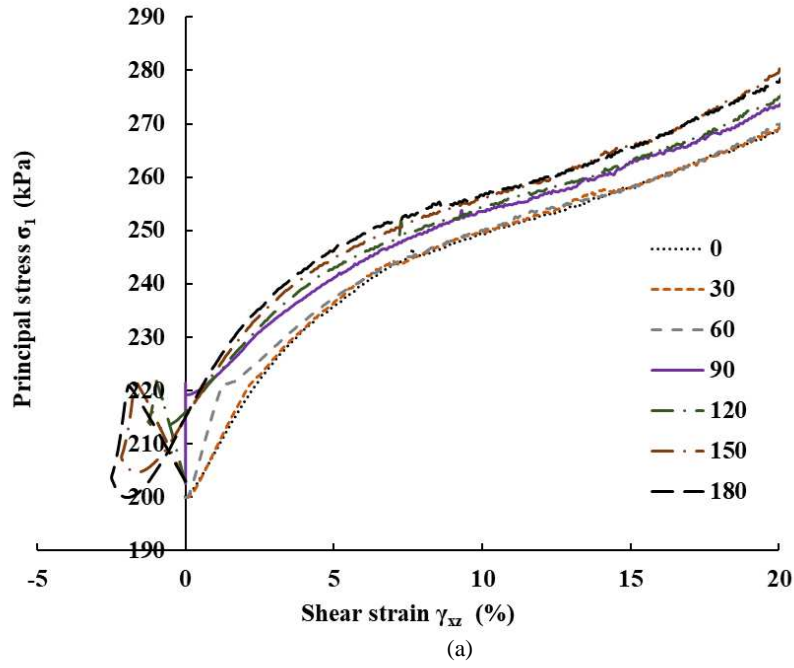


(a)



(b)

Fig. 6 Lateral normal stresses at different angles by the DEM (a: x-direction; b: y-direction)



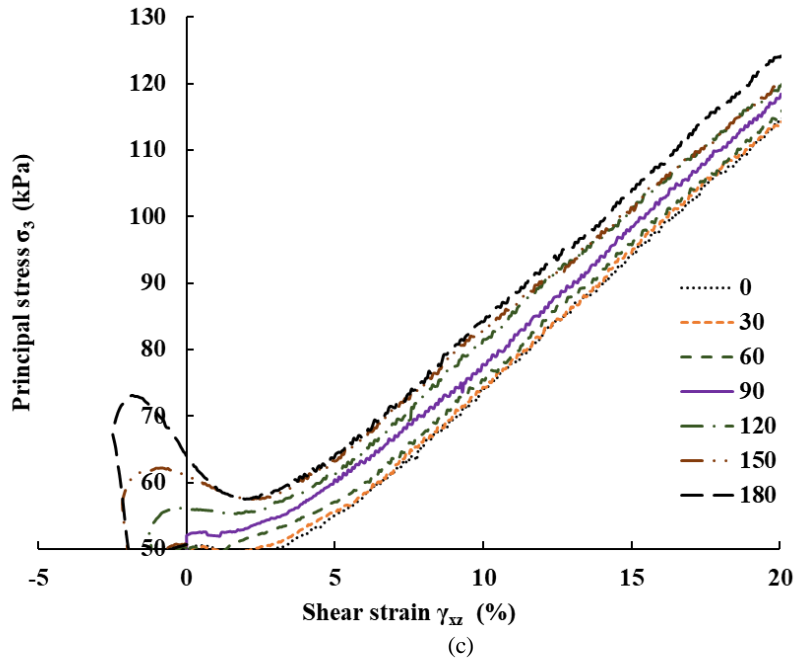


Fig. 7 Principal stresses at different loading angles by the DEM (a: major; b: intermediate; c: minor)

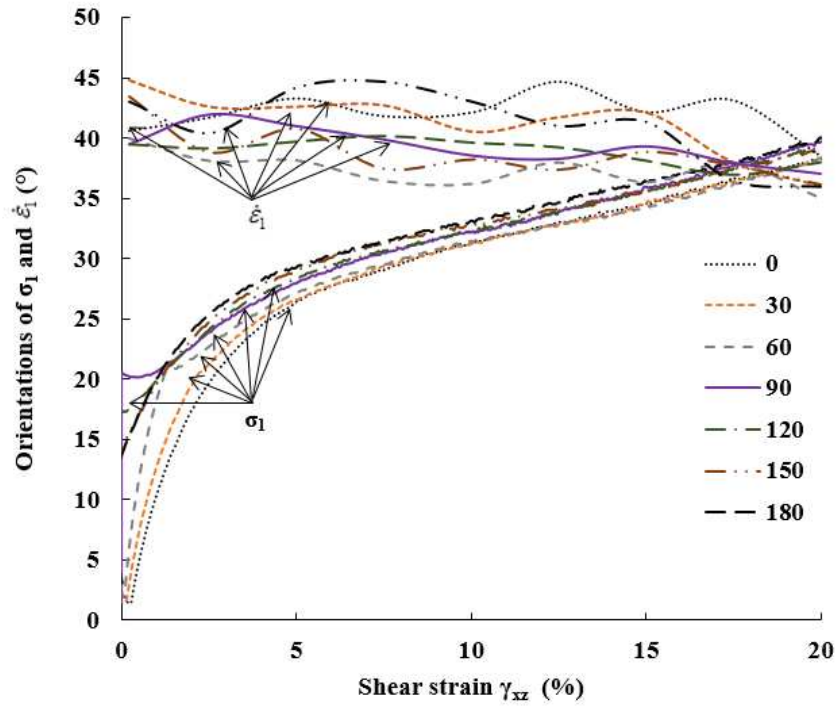


Fig. 8 Orientations of major principal stresses and principal rates at different loading angles by the DEM

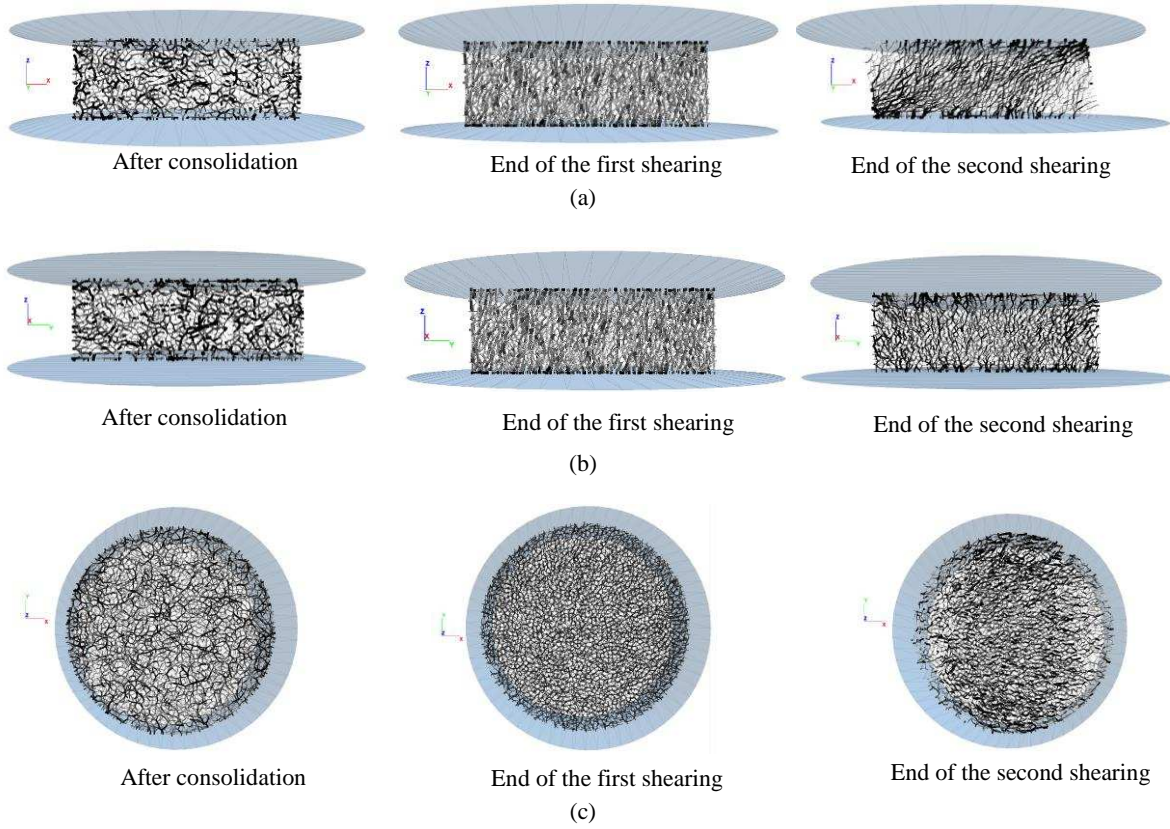


Fig. 9 Contact force chains of the 3D DEM model at the loading angle of 60° (a: front view (looking along the y-axis); b: side view (looking along the x-axis); c: top view (looking along the z-axis))

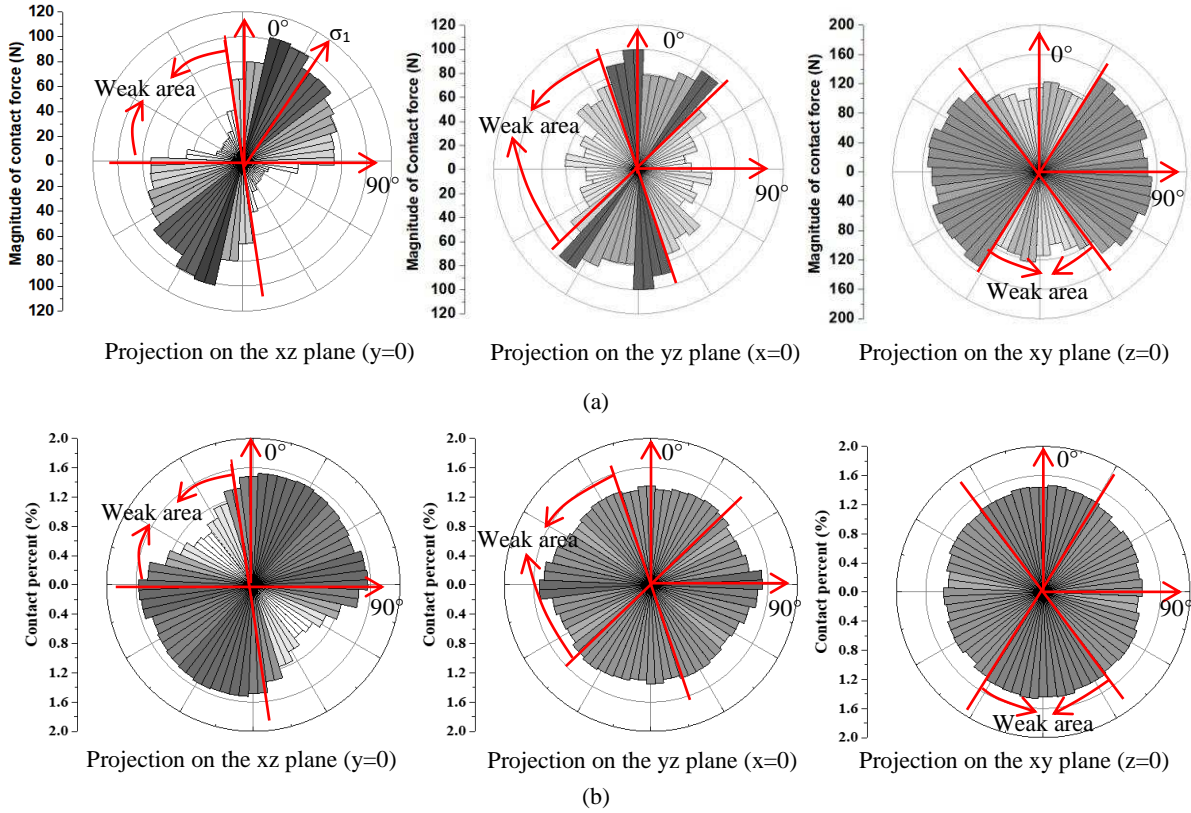


Fig. 10 Rose diagrams of the magnitude of contact forces (a) and contact normals (b) within the 3D DEM model by the end of the second shearing at the loading angle of 60°

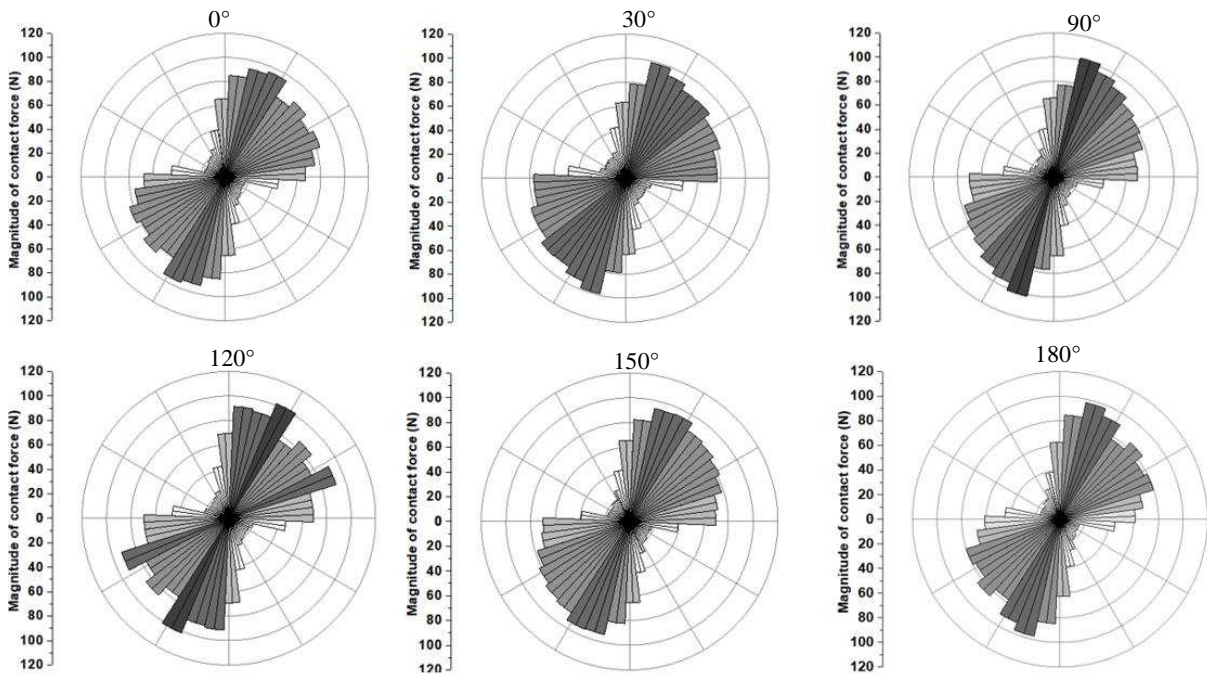


Fig. 11 Rose diagrams of the magnitude of contact forces projected on the xz -plane ($y = 0$) at the end of the second shearing at different loading angles

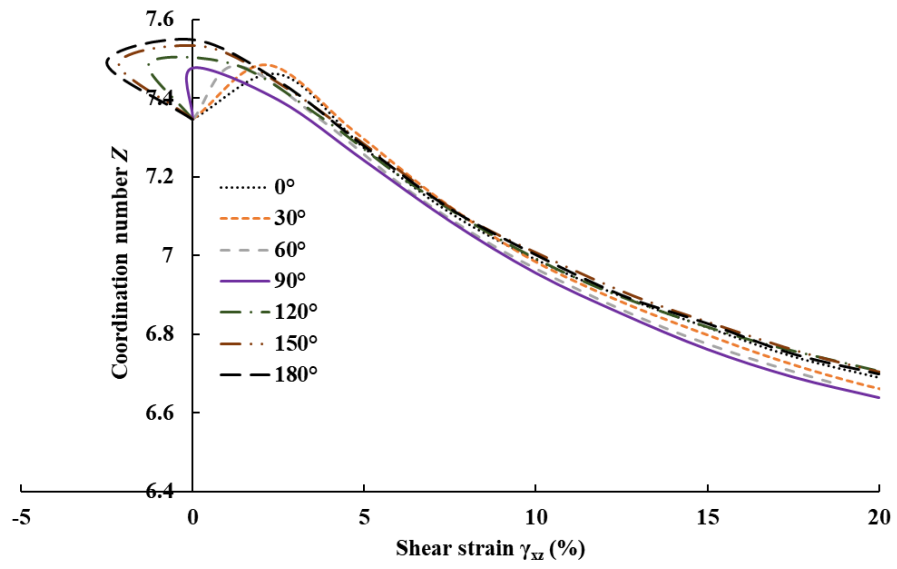
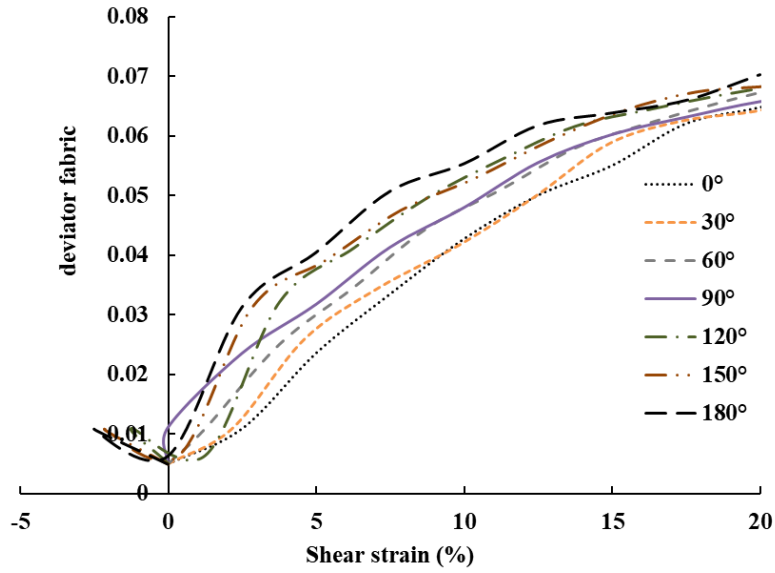
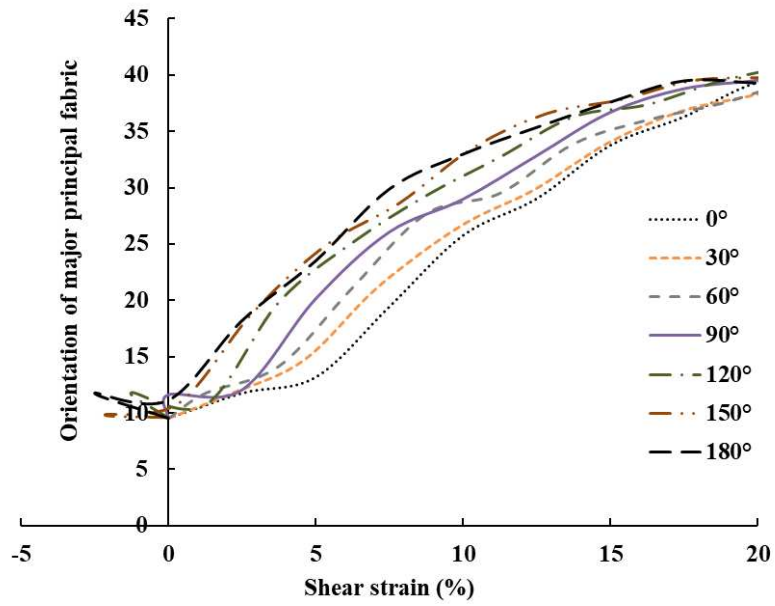


Fig. 12 Coordination number calculated by the DEM



(a)



(b)

Fig. 13. Deviator fabric (a) and orientation of the major principal fabric (b) at different loading angles by the DEM